Iranian Journal of Medical Physics

ijmp.mums.ac.ir

An Anthropomorphic Head Phantom Prototype for the Measurement of Geometric Distortion in Magnetic Resonance Imaging System

Sadegh Shurche[1*], Mohammad Yousefi sooteh[2]

1. Department of Medical Physics, Faculty of Medical Sciences, Tarbiat Modares University, Tehran, Iran
2. Department of Medical Physics, School of Medicine, Tabriz University of Medical Sciences, Tabriz, Iran

ARTICLE INFO

Article type:
Original Paper

Article history:
Received: Nov 22, 2022
Accepted: Apr 18, 2023

Keywords:
Anthropomorphic Head Phantom
Geometric Distortion
High-field MRI

ABSTRACT

Introduction: Our goal is to design and construct a new anthropomorphic head phantom for assessment of image distortion in treatment planning systems.

Material and Methods: In this study, CT scan images of heads were transferred to the Mimic software. Using this software, the skull texture was removed and a hollow layer was formed between the bone tissues, in which the bone tissue would be equivalent to the material. Then it was fabricated with a 3D printer using K_2HPO_4 (as bone). A new phantom containing 8,000 reference features (control points) with AutoCAD software designed, fabricated it with a 3D printer and filled it with gels that included nickel-doped agarose, urea, and sodium chloride (as soft tissue) and then placed this grid inside the head phantom. This phantom was tested on the Siemens 3 Tesla Prisma MRI model using a 64-channel head coil. In this regard, a three-dimensional reference model was used. Reproducibility on the phantom was investigated with three different imaging sessions per day for three different days.

Results: T_2 gel value, 84.804 ± 3ms was obtained for gel that simulates brain tissue. In addition, their corresponding T_1 measurements were 1090.92 (ms), respectively. By Adding nickel to agarose gels, the amount of CT number in all energies of 80 to 130 kVp increased. Increasing the concentration of nickel in gels results in a decrease in CT number. The geometric distortion in the 3D results was found to be due to field non-uniformity and nonlinearity of the gradients and its reproducibility.

Conclusion: The results show that, the amount of distortion in the middle of the field was less than that of its sides. This phantom can be used to check image distortion in treatment planning systems.

► *Please cite this article as:*
Shurche S, Yousefi sooteh M. An Anthropomorphic Head Phantom Prototype for the Measurement of Geometric Distortion in Magnetic Resonance Imaging System. Iran J Med Phys 2024; 21: 53-63. 10.22038/IJMP.2023.37141.1469.

Introduction

Stereotactic radiation therapy (SRS) relies heavily on imaging to accurately deliver large doses of radiation to small targets within the skull [1]. Therefore, the SRS effect strongly relies on the accuracy of its visual guidance, which is defined by visualizing the target and natural structures, as well as the geometric accuracy of their images [2].

The use of fast techniques with high contrast and high-resolution MRI has improved performance in SRS. One of the essential functions of the MRI device is to detect the exact location and size of the tumor [3].

One of the factors contributing to errors in delivering the intended doses to the tissues is the geometric error of MRI images. Geometric distortions in MRI can arise from various sources, including inherent magnetic field in homogeneities, nonlinearity of the gradient coils, and patient-induced distortions.

In general, the performance of MRI systems is directly related to the quality control (QC) of the tolerance levels maintained. However, optimizing performance and ensuring quality control requires time to calibrate and test the machine, which can be costly and negatively impact patient performance. This is particularly relevant for imaging centers that operate 24 hours a day, seven days a week, making it challenging to consistently perform QC tests.

Although QC tests are designed to evaluate the distortion of geometric images used in SRS treatment planning in several facilities, most MR QC tests are tailored to meet specific performance standards for diagnostic applications, not for more severe radiation therapy in general or SRS in particular.

Due to the high concentration of ionizing radiation in single doses used in SRS, it is essential to carefully assess the quality of each step in the delivery process to ensure precise targeting. This necessitates the implementation of a detailed QC program for the various components of the irradiation facility. In the case of MR systems used for SRS planning, a specific QC protocol should be followed in addition to the regular monthly MR service-testing, as an important supplement to the overall SRS-QC program [4].

*Corresponding Author: Tel: +98-2166466383; Fax: +98-+98-2188973653; Email: sadegh.shurche@yahoo.com

QC tests in MRI geometric distortion are generally intended to determine the spatial distortion of the MR image by routine imaging of test objects with specific geometric features. These are usually in the form of a cylindrical phantom or hydrostatic precipitate containing ACR MRI Quality Control Manual 2015, parallel array arrays [5] Capillary tube [6] or planes of the area are equally well-known in rectangular networks[7, 8].

We aim to present a 3D-phantom multifunctional design for QC evaluation of geometric image distortion of MR and CT images used for SRS treatment planning.

Materials and Methods

3D Phantom

Design Criteria

A phantom is required for geometric distortion assessment in SRS treatment planning. This phantom should have a distributed reference point that aligns accurately and precisely with known coordinates, both during the phantom's volume and when visualized in all three orthogonal imaging modes.

The workflow is shown in Figure 1, which highlights each step in the process to create an anthropomorphic phantom.

CT scan images used for designing head phantom

A phantom head design was used to design CT scan images of patients [9]. The best images of this collection were transferred to the Mimic software (Mimics® Innovation Suite). The sample CT image used to make the mold is shown in Figure 2.

Phantom head design

CT scan images were transferred to the Mimic software (Mimics® Innovation Suite). Using this software, the skull texture was removed and a hollow layer was formed between the bone tissues in which the bone tissue would be equivalent to the material. The designed phantom is shown in Figure 3.

Fabrication of head phantom

The Mimic software's head design was employed to create the Phantom. Kian Pars, a company based in Tehran, Iran, manufactured the Phantom using materials that are not sensitive to MRI magnetic field (figure 4). The magnetic properties, strength, and lightness of this material were utilized in its production [10]. A 3D printer in an Iranian company produced phantom.

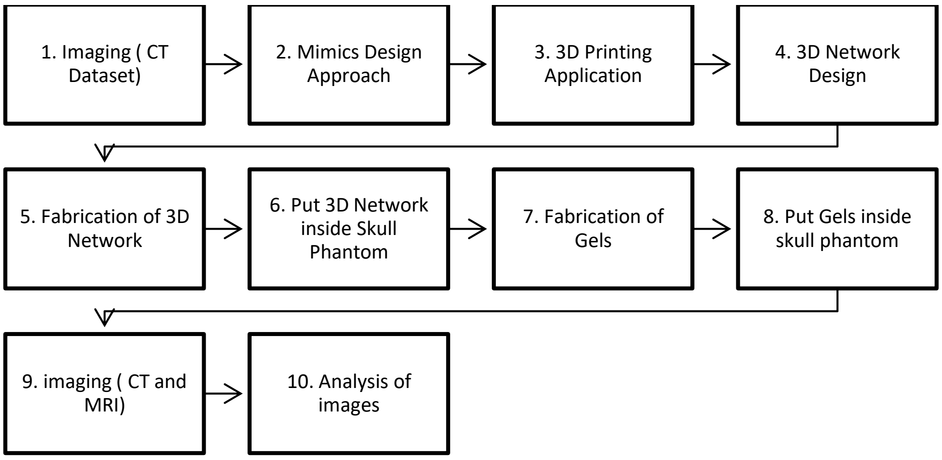

Figure 1. A General workflow to design and fabricate an anthropomorphic heterogeneous head phantom using 3D printing

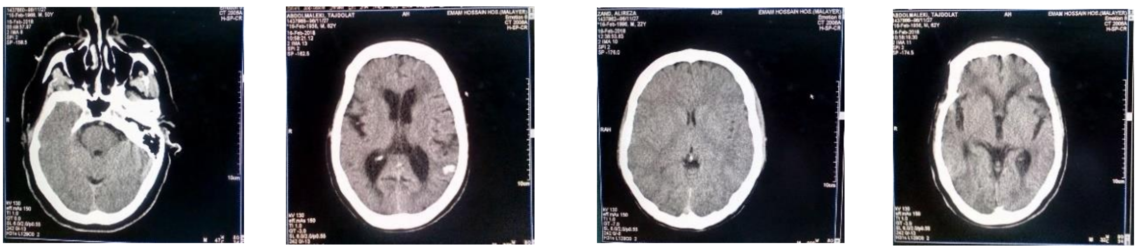

Figure 2. CT scan image samples used in phantom design. These images are taken using the 6-Slice Siemens CT scan device.

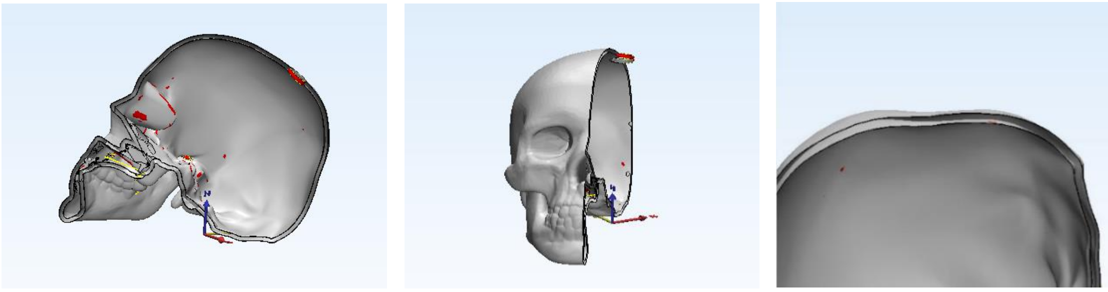

(a) (b) (c)

Figure 3. a) Lateral view of the phantom. b) The facade of Phantom. c) Blank layer between bone tissue.

(a) (b) (c)

Figure 4. (a) Phantom made using a 3D printer device. A hole is placed on the top of the phantom where the injection site is located. Weight of this phantom is 1.9 kg (b) Special pads enable use with all fixation frames. (c) Installing special pads from superior view.

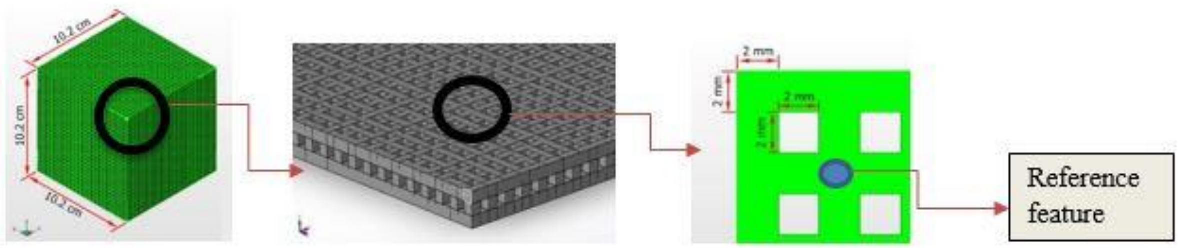

Figure 5. Phantom geometric distortion that was designed using software. The points where the lines meet were used to make a 3D model. The phantom consists of 20 pages, each 20×20 point reference page, with 8000 phantom reference points. The place where the lines meet covers a volume of 2 × 2 × 2 mm.

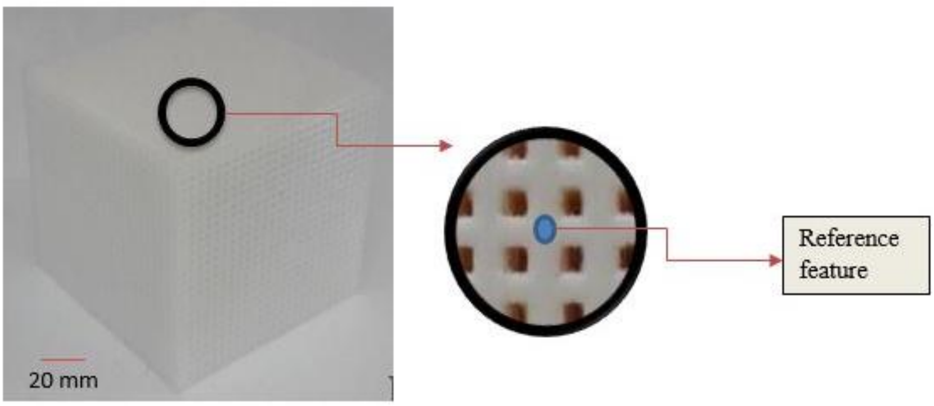

Figure 6. Geometric distortion phantom built using a 3D printing method.

3D grid phantom design

In our previous paper, we examined two-dimensional geometric displacement using appropriate phantoms, then we designed a 3D phantom to investigate geometric displacement[11]. We used this three-dimensional phantom in phantom head construction. This 3D network includes 8,000 reference features in whole head phantom. In this study, a phantom measuring 90 x 90 x 90 mm was designed in three dimensions using the software (Figure 5). The phantom was made using materials that do not react to the magnetic field in the MRI machine (figure 6).

Phantom material

Gel used in phantom

In order to simulate brain tissue, we used the gel we created in our previous papers [11], to test the amount of T_1, T_2, and ADC in the Tesla MRI 3 machine. We, also, used this gel to check the accuracy and repeatability of ADC in 1.5 Tesla devices.

The concentrations of nickel, agarose, and sucrose used to make the gels, which were then used to fill the respective phantom compartments, are detailed in Table 1.

Substitute bone matter

The bone matter of the phantom is replaced with a surrogate that mimics cranial bone using a solution of dipotassium phosphate in distilled water. Dipotassium phosphate solutions allow for the adjustment of electron densities similar to those of bone for CT and have a chemical composition similar to bony tissues. Heating the water to 50°C helps to dissolve the elevated concentration of dipotassium phosphate in water [12].

The phantom was placed on a shaking plate for three minutes immediately after filling. The process was conducted to avoid the capture of air bubbles in the phantom, which might cause susceptibility artifacts.

Phantom imaging

CT scan imaging for geometric distortion

The control point locations were established by conducting a CT scan of a phantom using a Siemens 6 Slice CT scan device. The phantom was placed at the center of the CT scan bed, with an in-plane resolution of 0.5 x 0.5 mm and a resolution outside the plane of 1 x 1 mm. This process was used to determine the precise positions of the control points for the subsequent procedures

CT scan imaging for material characterization

The head phantom was scanned using a CT scanner (Siemens) with the following settings:

- Tube voltages: 80 kVp and 120 kVp
- Tube currents: 220 mAs (80 kVp) and 85 mAs (120 kVp)
- Default pitch: 0.6
- Rotation time: 1 second

Three-millimeter slice images were reconstructed using a D30 kernel.

The researchers have proposed two formulas linking the relative electron density (reD) of human body tissues to their corresponding CT numbers. These formulas are based on the tissue's nature, with properties similar to water or bone in terms of Hounsfield units (HU). For soft water-like tissues with a low atomic number (Z) and a CT number (NCT) of <100, the electron density (ρ_e) was determined [13, 14]

$$\rho_e=1.0+(0.001\times N_{CT}) \quad (1)$$

For bone-like tissues with higher Z values, such that N_{CT} is >100, ρ_e is defined as

$$\rho_e=1.052+ (0.00048\times N_{CT}) \quad (2)$$

Therefore,

$$\text{Relative electron density}=\rho_e/\rho_{(e,water)} \quad (3)$$

Relative electron densities, reD_{CT}, were calculated using equations (1) and (2) from the mean CT numbers for the CT scanners per material.

Table 1. Materials used to make phantom gel.

Gel in order to simulate brain tissue	Agarose concentration (% w/v)	Sucrose concentration (% w/v)	Nickel concentration (mM)
	1.2	-	1.8

Table 2. Particularity of scanner used in this study. Parameters taken from the system manual.
(GS: Gradient Strength, SR: Slow Rate)

Vendor	Model	Field(T)	GS(mT/m)	SR(T/m/s)	Homogeneity(ppm)	Diameter(cm)	Length(cm)
Siemens	prisma	3	80	200	1.1 typical[1]	60	213

[1]At 24 cm diameter spherical volume (DSV)

Table 3. The imaging parameters used in this study.
(FA: Flip Angle, TR: Repetition Time, TE: Echo Time, FOV: Field of View, NEX: Number of Excitations)

Sequence	TR/TE(ms/ms)	FA(^{0})	FOV(mm×mm)	In plane Resolution(mm×mm)	Slice width(mm)	Receiver Bandwidth(Hz/Pixel)	Number of Excitations
3D FLASH	11/5	30	250 × 250	0.71×0.71	1	285	1

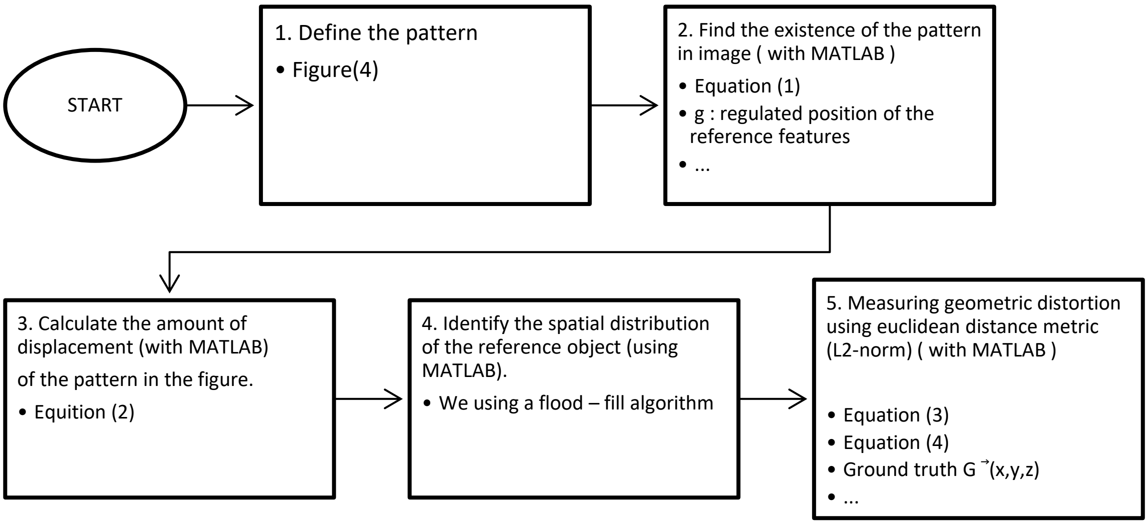

Figure 7. Image analysis steps. Image analysis was carried out in the five steps mentioned in the flowchart.

MR imaging

A phantom, designed for quality assurance of the spatial accuracy of MRI, was positioned along the B_0 field axis with supports to ensure reproducible placement. The imaging was conducted using a 3-Tesla Prisma MRI at the NBML (Iran). The scanner had a 64-channel head coil and used 3D gradient echo techniques, such as 3D FLASH. The details of the scanner and imaging parameters are provided in the respective tables (Table 2&3) [15]. 3D FLASH is a technique that enables the acquisition of high-resolution, high-contrast, thin-section T_1-weighted images of the body [15]. The imaging device utilized a distortion modifier filter, and each imaging session lasted 10 minutes, with an average imaging time of 30 minutes per day. When using a phantom, it is crucial to know its relaxation times, particularly T_1, to choose the pulse sequence parameters. The amount of T_1 and T_2 gels in the phantom was measured using an inversion recovery sequence and a multi-echo sequence, respectively, on the machine to determine the relaxation times [16]. Both data series were fitted using a mono-exponential model.

Analysis of images

Detection of reference feature

Since normalized cross correlation (NCC) algorithm [17] is strong and a generally used likeness measure in image processing this algorithm was used. The images were analyzed using MATLAB software. The steps of analyzing the images are shown in Figure 7.

We Using NCC[18] regulated the position of a reference features in a three-dimensional image (g). Let g(x,y,z) indicate the intensity value of the image volume (g) of the size $M_x \times M_y \times M_z$ at the point (x,y,z) where $x \in \{0, . . . , M_x - 1\}$, $y \in 0, . . . , M_y - 1$, $z \in \{0, . . . , M_z - 1\}$. A given pattern (p) of the size Nx × Ny × Nz used to represented the pattern.

The normalized cross-correlation value (τ) is a measure used to determine the similarity between a template pattern (p) and an image (g) at different positions. It is calculated at each point (u, v, w), where the pattern (p) is shifted by u steps in the x-direction, v steps in the y-direction, and w steps in the z-direction. This measure is commonly used in image processing for tasks such as template matching and image registration.

The definition for NCC can be expended from 2D to a third dimension and be expressed as:

$$\tau = \frac{\sum_{x,y,z}(g(x,y,z)-\bar{g}_{u,v,w})(p(x-u),y-v,z-w)-\overline{p})}{\sqrt{\sum_{x,y,z}(g(x,y,z)-g_{u.v,w})^2 \sum_{x.y.z}(p(x-u,y-v,z-w)-\bar{p})^2}} \qquad (4)$$

Where $(\overline{p})$ is the mean value of the pattern (p), $\bar{g}_{u,v,w}$ denotes the mean value of g(x, y, z) within the area of the pattern (p) shifted to (u, v, w) and is calculated by:

$$\bar{g}_{u,v,w} = \frac{1}{N_x N_y N_z} \sum_{x=u}^{u+N_x-1} \sum_{y=v}^{v+N_y-1} \sum_{z=w}^{w+N_z-1} g(x,y,z) \qquad (5)$$

While NCC is a computationally expensive algorithm, it can be estimated using Fourier-based techniques or the sum-table method [18, 19]. Template matching is an efficient CPU function that calculates the matching score between a template and a (color) 2D image or 3D image volume. It computes:

- The sum of squared differences (SSD Block Matching), which is a robust template matching method.
- The normalized cross correlation (NCC), which is independent of illumination and only dependent on texture.

By combining the two images, users can achieve template matching that works robustly with various applications. Both matching methods are implemented using FFT-based correlation.

In the given application, the reference feature (Figure 8) is a well-defined feature, so an approximation is sufficient to distinguish it from the background as well as horizontal and vertical edges. The pattern's origin was determined by examining the central vertex within a 5x5x5 voxel pattern extracted from the CT and MR acquisitions. It was assumed that this point in space was free of distortions in the MR acquisition, as it is located in the magnet isocenter [20].

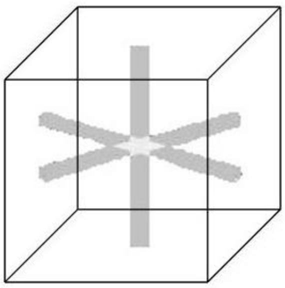

Figure 8. Schematic shape of the reference feature used in normalized cross correlation.

Detection of the Spatial Distribution of the reference feature

The NCC algorithm's coefficients were utilized as the volume for each voxel traversed in the algorithm. The NCC coefficients were then thresholded to retain only the highest correlating points that corresponded to the reference feature. The reference feature was determined using a connected-component approach, where connected image pixels were labeled in groups using a flood-fill algorithm [21].

Error value

The process of calculating the displacement distance of a reference point using a CT scan image as the ground truth and the Euclidean distance metric to measure the geometric displacement using equation (6 and 7).

$$\vec{G}(x,y,z) = (x,y,z) \qquad (6)$$

$$d(x,y,z) = ||\vec{G}(x,y,z) - \vec{C}(x,y,z)||_2, (x,y,z) \in B^3$$
[22]

Reproducibility measurement

A measure of distortion repeatability was calculated by measuring the mean and standard deviation of distortion and applying the equation (8,9 and 10) [23]:

$$Mean = \sum_{i=1}^{n} \frac{D_i}{n} \quad [12]$$

$$standard\ deviation = \sqrt{\sum_{i=1}^{n} \frac{(D_i - Mean)^2}{n-1}} \qquad (9)$$

$$CV = \frac{Standard\ deviation}{Mean} \qquad (10)$$

The formula for calculating geometric error is given as $D_i = n$, where i is the geometric error and n is the number of geometric displacement measurement locations. To assess the reproducibility of the procedure in the Siemens Scanner, imaging was repeated three times in one day without removing and replacing the phantom (CV_1), and on three different days with removal and replacement of the Phantom (CV_2) when the phantom was completely placed within the brain coil. It is expected that the value of CV_1 will be less than five percent and less than that of CV_2.

Results

Properties of gels in CT scan and MRI

T_2 gel value, 84.804 ± 3ms was obtained for gel that simulates brain tissue. In addition, their corresponding T_1 measurements were 1090.92 (ms), respectively.

By Adding nickel to agarose gels, the amount of CT number in all energies of 80 to 130 kVp increased. Increasing the concentration of nickel in gels results in a decrease in CT number. This gel behavior is similar to body tissues, such as muscle and brain[12]. CT number for gel agarose and nickel are between 34-54 and have many similarities to real brain tissue. Degree of electron density for gel 23 is 1.042, which is slightly larger than that of real brain tissue.

CT imaging of phantom

CT images of head phantom without gels, substitute bone matter and grid of geometric distortion are shown in Figure 9, while CT images of head phantom with gels, substitute bone matter and grid of geometric distortion are shown in Figure 10. 3D image reconstructions from different views of the head phantom without gels, substitute bone matter and grid of geometric distortion are shown in Figure 11.

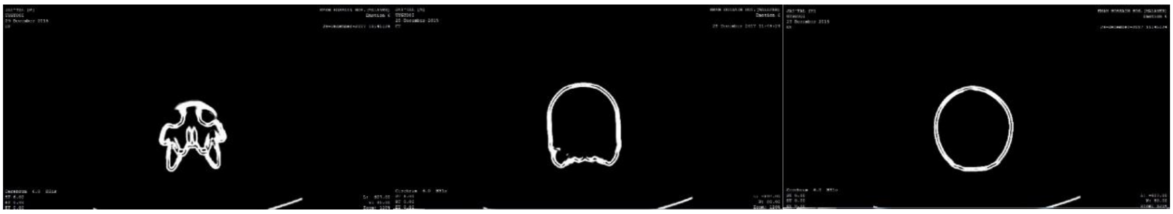

Figure 9. Different sections of the head phantom are taken using the Siemens 6 Slice CT Scanner. At this point, the phantom is empty.

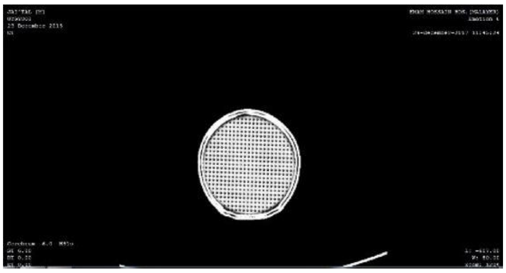

Figure 10. Sections of the head phantom are taken using the Siemens 6 slice CT scanner. At this point, the phantom includes gels; substitutes bone matter and grid of geometric distortion.

(a) (b) (c)

Figure 11. 3D image reconstruction from different views of the head phantom with gels, substitutes bone matter and grid of geometric distortion taken by the Siemens 6 Slice CT Scanner. a) Lowered view of phantom b) anterior view of phantom c) lateral view of phantom.

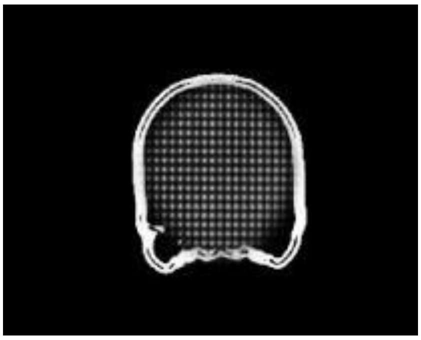

Figure 12. Sections of the head phantom are taken using the Siemens 6 slice CT scanner. At this point, the phantom includes gels; substitutes bone matter and grid of geometric distortion.

MR imaging of phantom

MR images of head phantom without gels, substitute bone matter and grid of geometric distortion are shown in Figure 12.

Geometric distortion

The CT scan generated a 3D image without any artificial distortions. A 3D image was created using software, and reference points were compared with MRI and CT images to calculate the error rate. Figure 13 shows the error volumes associated with the study. The average error in the MRI volume's Euclidean distance was less than 1mm, with a maximum error of 1.5 mm, consistent with studies [27] and the manufacturer's specifications. The overall volume exhibits noticeable distortion, especially at the periphery of the magnetic field. The geometric distortion in millimeters for the axial reference point planes of the object on three different days is depicted in figure 14.

Tables 4 and 5 demonstrate the reproducibility of image non-uniformity in a device, measured in three directions: x, y, and z.

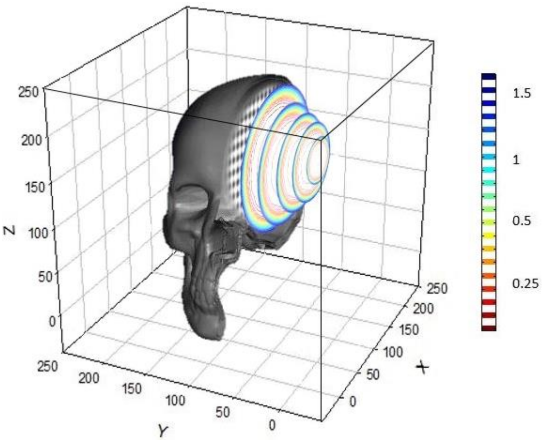

Figure 13. The amount of geometric displacement of the phantom's reference point in millimeters. According to the image, the distortion value increases outward from the center of the field.

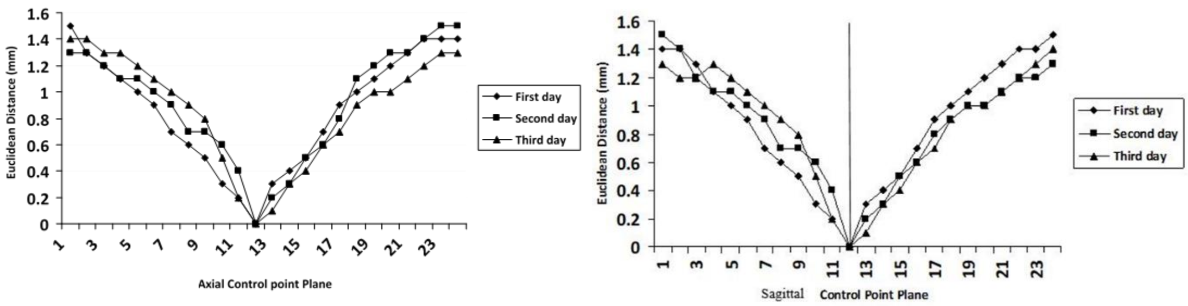

Figure 14. Amount of geometric displacement in images. a) Amount of displacement in the first, second and third days in the axial direction, b) amount of displacement in the first, second and third days in the sagittal direction.

Table 4. The results obtained from measuring the reproducibility of image non-uniformity in a device in three directions, namely x, y, and z, which is represented by CV1.

Protocole	Percent of distortion in x axises (mean ±s.d)(1)	Percent of distortion in y axises(mean±s.d)(1)	Percent of distortion in z axises(mean±s.d)(1)
3D FLASH	1.6 ± 0.5	1.5 ± 0.3	1.7 ± 0.2

Table 5. Results of measuring the Reproducibility of image non-uniformity in the device in both directions of x and y (CV2)

Protocole	Percent of distortion in x axises (mean ±s.d)(2)	Percent of distortion in y axises(mean±s.d)(2)	Percent of distortion in z axises(mean±s.d)(2)
3D FLASH	1.7 ± 0.2	1.8 ± 0.2	1.9 ± 0.3

Discussion

The article introduces a three-dimensional phantom created with a 3D printer to assess image distortion in treatment planning systems.

The success of SRS relies heavily on the uniqueness of visualization and target localization in the stereotactic space, which is determined by the combined imaging techniques for SRS, as well as the precision of dosage and delivery dose measurement. This means that the accuracy of SRS is significantly influenced by the individualized approach to visualizing and locating the target in the stereotactic space, as well as the precise measurement of the dosage and its delivery [24].

With the advent of MRI as the main method for detecting intracranial tumors, the accuracy of target localization in SRT planning has improved significantly. This advancement requires the appropriate non-linear gradient and geometric distortion derived from the MRI images used in SRT treatment planning [25].

The usual method for checking image distortion involves taking measurements from known distances between internal reference points or radial measurements along the phantom diameter using a manual measurement tool. However, this method is prone to errors and only provides an approximate estimate of the distortion error. It is also limited to the diameter of the phantom and a small number of reference points. The 3D phantom described in Figures 2 and 3 overcomes these limitations and has several advantages.

This phantom is particularly interesting due to several of its features that set it apart from other available phantoms. One notable aspect is the MRI-positive/CT-negative (1 cm) 3D-Cartesian network, which allows for the assessment of image distortion in the axial, coronal, and sagittal imaging screens without the need to rotate or move the phantom. This is made possible by the signal network convergence in all three main directions, a key feature that enables the measurement of distortion on the page and through the page.

The 2 mm grid spacing in three dimensions means that image sets consist of grid planes separated by 2D arrays of signal points, as shown in Figure 12. This design allows for easy visualization of image distortion on MR consoles, where brighter-signal regions from neighboring grid planes can be observed to be warped into adjacent image slices, particularly noticeable in the Coronal images of Figure 12.

The SRS MR Distortion Phantom is a tool that can assess image distortion on the actual imaging plane and on the reconstructed images. The distortion values for each vertex coordinate can be reformatted into planes orthogonal to the acquisition-imaging plane, allowing for quantitative and color-coded distortion evaluation of the reconstructed images. This feature is useful for MR-images acquired in one image-plane and then reconstructed into orthogonal planes, with all three then used for SRS treatment planning.

This particular ghost has several unique features. Firstly, the reference points in this phantom were 2 mm apart in the 3 directions, while other research have reported larger gaps. The average distortion error in this research was less than 1.5 mm. Additionally, the plate design of the phantom makes its shape perfectly suitable for comprehensive 3D analysis using different coils, as the number of plates is easily adjustable, allowing a single device with several series of plates of different sizes to fit several FOVs.

The combination of materials that are compatible with magnetic fields and gels in a phantom provides a suitable and realistic imaging environment for CT scan imaging, enabling the identification of reference points and accurate assessment of imaging parameters. The accuracy of a 3D printer is also demonstrated in the image, as shown in Figures 9, 10, and 11.

According to the data in Figures 12, the utilization of impermeable materials that are compatible with magnetic fields and gels in this model is appropriate for MR imaging, and markers can be recognized in the resulting image. Furthermore, the image demonstrates the precision of a 3D printer.

According to figures, 13 and 14, Euclidean distance errors have been observed in the corners of the phantom, which can be attributed to several factors. These include non-linearity in the gradient, non-homogeneity in B_1 and B_0, or the susceptibility of magnetic properties at the interface between the phantom and air. To mitigate the susceptibility of magnetic properties in the phantom and air interface, the phantom was enclosed within a leak-tight container.

Our previous research on this device suggests that these errors may stem from:

- Non-homogeneity in B_1 and B_0 of MRI [26]
- Non-linearity of the gradient

These factors can cause errors in the corners of the phantom, leading to undesirable artifacts and affecting the accuracy of the MRI measurements. By addressing these issues, researchers can improve the performance of MRI systems and obtain more accurate results for various applications.

Our study revealed that the CT numbers and relative electron density of gels that include nickel-doped agarose, urea and sodium chloride (as soft tissue) and K_2HPO_4 (as bone) indicate that the gels have the potential to be used as tissue substitutes, which is consistent with the results of Gallas et. al[27] The gels are made of readily available, cost effective, and nontoxic materials.

The research conducted in this area, along with other investigations, found that the distortion in the center of the field was lower than the distortion at the edges [28]. This issue can be shown in figures 13 and 14.

The reproducibility measurement results for geometric distortion, as shown in Tables 4 and 5, suggest that CV_1 is expected to be less than CV_2, and both are expected to be less than 5%.

Among the problems that we encountered in the phantom design, which should be considered in the following studies, are; the space left to fill the bone-like material is small; the phantom is divided into two halves to insert a three-dimensional network into it which caused problems. In addition, the material used to make the bone similar was fluid, so the phantom head should be carefully sealed.

The use of the centroid algorithm in distortion analysis was improved by the positive MR signal design, which enhances the accuracy of the algorithm. The centroid algorithm evaluates pixel signal intensity in the region encompassing the vertex to find the center of mass, and it is highly sensitive to variations in pixel values. The highest pixel intensities are found near the center of an intersection, with a 10-20% decrease in pixel intensity observed at the edges. The greater the difference between edge and center pixel intensity values, the more accurate the analysis. However, a negative signal decreases the difference between pixel intensities near the center of the vertex and the edges, leading to reduced accuracy using the centroid algorithm.

In order to achieve accurate results using a 3D phantom, it is essential to consider the imaging protocol's sequence parameters, which should reflect the requirements of stereotactic precision and the actual sequences used clinically. Key factors to consider include:

- Slice Thickness: Images should be acquired with a slice thickness of 1.0 – 1.5mm.
- Field-of-View: The field-of-view should be between 230 – 250 mm.
- Bandwidth: The bandwidth should be ≥ 15 kHz.
- Imaging Matrix: The imaging matrix should have at least 256 x 256 points.

Increasing the sampling matrix size to 384 x 384 or 512 x 512 would improve image resolution, but at the cost of increased imaging time. However, this may not substantively improve analysis accuracy.

The phantom itself may cause image distortion due to susceptibility differences between interfaces, but these effects are expected to be smaller compared to those observed at patient interfaces.

In conclusion, the 3D FLASH sequence utilized in these assessments is representative of a typical T_1-weighted Gradient Echo sequence, which is our most frequently used volumetric MR sequence for SRS treatment planning. The specific outcomes of time-course assessments may vary depending on the pulse sequence and MR manufacturer.

In the following steps, we aim to construct a phantom like this but with a larger and apply this to correct geometric distortions in treatment planning.

Conclusion

QC MRI tests designed for diagnostic imaging are not enough to meet the demands of the SRS program; therefore, a more precise method capable of evaluating the distortion of the MR image is required on all imaging planes. To this end, the design and application of a 3D multi-dimensional phantom for quantitative evaluation of the geometric accuracy of the MRI / CT images were used to plan the stereotactic radiotherapy treatments. We have also shown how this device may run as part of the MR / CT imaging QC section of an overall SRS QC program. This multipurpose 3D phantom facilitates the evaluation of gradient stability over time, in addition to the presentation of targeting accuracy evaluation, and as a result, we presented a quantitative method for demonstrating the reliability of the geometric accuracy of the MR / CT images used to plan the SRS**.**

References

1. Alexander E, Loeffler JS, Lunsford LD. Stereotactic radiosurgery. 1993.
2. Schell MC, Bova FJ, Larson DA, Leavitt DD, Lutz WR, Podgorsak EB, et al. Stereotactic Radiosurgery: AAPM Report No 54. Radiation Therapy Committee Report of Task Group. 1995;42.
3. Zhang B, MacFadden D, Damyanovich AZ, Rieker M, Stainsby J, Bernstein M, et al. Development of a geometrically accurate imaging protocol at 3 Tesla MRI for stereotactic radiosurgery treatment planning. Physics in Medicine & Biology. 2010 Oct 20;55(22):6601.
4. Nutting C, Brada M, Brazil L, Sibtain A, Saran F, Westbury C, et al. Radiotherapy in the treatment of benign meningioma of the skull base. Journal of neurosurgery. 1999 May 1;90(5):823-7.
5. Walton L, Hampshire A, Forster DM, Kemeny AA. A phantom study to assess the accuracy of stereotactic localization, using T1-weighted magnetic resonance imaging with the Leksell stereotactic system. Neurosurgery. 1996 Jan 1;38(1):170-8.
6. Sumanaweera TS, Adler Jr JR, Napel S, Glover GH. Characterization of spatial distortion in magnetic resonance imaging and its implications for stereotactic surgery. Neurosurgery. 1994 Oct 1;35(4):696-704.
7. Price RR, Axel L, Morgan T, Newman R, Perman W, Schneiders N, Selikson M, Wood M, et al. Quality assurance methods and phantoms for magnetic resonance imaging: report of AAPM nuclear magnetic resonance Task Group No. 1. Medical physics. 1990 Mar 1;17(2):287-95.
8. Mack A, Wolff R, Scheib S, Rieker M, Weltz D, Mack G, et al. Analyzing 3-tesla magnetic resonance imaging units for implementation in radiosurgery. Journal of Neurosurgery. 2005 Jan 1;102(Special_Supplement):158-64.
9. DICOM Library - Anonymize, Share, View DICOM files ONLINE [Internet]. www.dicomlibrary.com. Available from: https://www.dicomlibrary.com.
10. Filippou V, Tsoumpas C. Recent advances on the development of phantoms using 3D printing for imaging with CT, MRI, PET, SPECT, and ultrasound. Medical physics. 2018 Sep;45(9):e740-60.
11. Shurche S, Yousefi Sooteh M. Fabrication of New 3D Phantom for the measurement of Geometric Distortion in Magnetic Resonance Imaging System. Iranian Journal of Medical Physics. 2019 Sep 1;16(5):377-84.
12. Bryant JA, Drage NA, Richmond S. CT number definition. Radiation Physics and Chemistry. 2012 Apr 1;81(4):358-61.
13. Thomas SJ. Relative electron density calibration of CT scanners for radiotherapy treatment planning. The British journal of radiology. 1999 Aug;72(860):781-6.
14. Claude KP, Schandorf C, Amuasi JH, Tagoe SN. Fabrication of a tissue characterization phantom from indigenous materials for computed tomography electron density calibration: peer reviewed original article. South African Radiographer. 2013 May 1;51(1):9-17.
15. Runge VM, Wood ML, Kaufman DM, Nelson KL, Traill MR. FLASH: clinical three-dimensional magnetic resonance imaging. Radiographics. 1988 Sep;8(5):947-65.
16. Tofts PS, Du Boulay EP. Towards quantitative measurements of relaxation times and other parameters in the brain. Neuroradiology. 1990 Sep;32:407-15.
17. Gonzalez RC. Digital image processing. Pearson education india; 2009.
18. Briechle K, Hanebeck UD. Template matching using fast normalized cross correlation. InOptical Pattern Recognition XII. 2001 Mar 20; 4387: 95-102.
19. Crow FC. Summed-area tables for texture mapping. InProceedings of the 11th annual conference on Computer graphics and interactive techniques. 1984 Jan 1; 207-12.
20. SJ D. A complete distortion correction for MR images: I. Gradient warp correction. Phys Med Biol. 2005;50:2651-61.
21. Vincent L. Morphological grayscale reconstruction in image analysis: applications and efficient algorithms. IEEE transactions on image processing. 1993 Apr;2(2):176-201.

22. Chung J, Hulbert G. A time integration algorithm for structural dynamics with improved numerical dissipation: the generalized-α method.
23. Mizowaki T, Nagata Y, Okajima K, Kokubo M, Negoro Y, Araki N, et al. Reproducibility of geometric distortion in magnetic resonance imaging based on phantom studies. Radiotherapy and Oncology. 2000 Nov 1;57(2):237-42.
24. Barbosa NA, da Rosa LA, Batista DV, Carvalho AR. Development of a phantom for dose distribution verification in Stereotactic Radiosurgery. Physica Medica. 2013 Sep 1;29(5):461-9.
25. Weygand J, Fuller CD, Ibbott GS, Mohamed AS, Ding Y, Yang J, et al. Spatial precision in magnetic resonance imaging–guided radiation therapy: the role of geometric distortion. International Journal of Radiation Oncology* Biology* Physics. 2016 Jul 15;95(4):1304-16.
26. Shurche S. Measurement of Radio Frequency Non-Homogeneity in MRI. Measurement. 2018;12(4).
27. Gallas RR, Hünemohr N, Runz A, Niebuhr NI, Jäkel O, Greilich S. An anthropomorphic multimodality (CT/MRI) head phantom prototype for end-to-end tests in ion radiotherapy. Zeitschrift fuer Medizinische Physik. 2015 Dec 1;25(4):391-9.
28. Orth RC, Sinha P, Madsen EL, Frank G, Korosec FR, Mackie TR, et al. Development of a unique phantom to assess the geometric accuracy of magnetic resonance imaging for stereotactic localization. Neurosurgery. 1999 Dec 1;45(6):1423.